Nonlinear Dyn (2011) 63: 35–49
DOI 10.1007/s11071-010-9783-6

ORIGINAL PAPER

Nonlinear dynamics of a new electro-vibro-impact system

Jee-Hou Ho · Van-Du Nguyen · Ko-Choong Woo

Received: 21 January 2010 / Accepted: 11 July 2010 / Published online: 8 August 2010

Abstract A variety of nonlinear dynamic responses for a new electro-vibro-impact system is presented, with indication of chaotic behavior. By mathematical modeling of the physical system, an insight is obtained to the global system dynamics. The modeling has established a good correlation with experimental data, and hence can be used as a numerical tool to optimize the system dynamics. In particular, with respect to impact forces and progression rate, may then be achieved with minimal computational cost.

Keywords Electro-vibro-impact system · Chaos · Mathematical model

J.-H. Ho (✉)
Faculty of Engineering and Science, Universiti Tunku Abdul Rahman, Jalan Genting Kelang, 53300 Setapak, Kuala Lumpur, Malaysia
e-mail: hojh@utar.edu.my

V.-D. Nguyen
Thai Nguyen University of Technology, 3-2 Street, Thai Nguyen City, Viet Nam
e-mail: vandu@tnut.edu.vn

K.-C. Woo
Faculty of Engineering, The University of Nottingham Malaysia Campus, Jalan Broga, 43500 Semenyih, Selangor Darul Ehsan, Malaysia
e-mail: Woo.Ko-Choong@nottingham.edu.my

1 Introduction

Applications of vibro-impact mechanical systems occur in many branches of technology such as percussive drilling, ultrasonic machining and ground moling [1]. Such systems are inherently nonlinear due to the presence of the non-smooth or discontinuous system characteristics. Despite the fact that some systems are relatively simple in its structure, very complex system dynamics have been revealed. Examples of such systems are piecewise linear impact oscillators [2–4], whereby its behavior may vary from periodic to chaotic motion. Peterka [5, 6] studied the bifurcations and transition phenomena in mechanical systems with impacts.

Due to the complexity of vibro-impact systems, a combination of analytical and numerical methods was used in several studies. A precise mathematical model is required in order to study the qualitative dynamic responses of the system. Wiercigroch [7] showed two methods to model dynamical systems with discontinuities. The first approach is to model the system using discontinuous functions. Global solution is obtained by "gluing" local solutions obtained by solving the problem in the continuous subspaces. The second approach uses smoothening functions to model discontinuous systems. Pavlovskaia et al. [8, 9] developed a semi-analytical method to compute periodic solutions for an impact oscillator with a drift. The motion could be subdivided into a sequence of distinct phases whereby the analytical solution for each phase is known. Chatterjee et al. [10] applied the har-

monic balance method to study a model of the impact damper containing symmetric stops. Both elastic and inelastic collisions were analyzed and refined numerically. Barrientos and Baeza [11] simulated the impact between two rigid bodies. Simulations, in the form of animations of objects in impact, were completed using a Runge–Kutta method in Matlab. Hinrichs et al. [12, 13] investigated two types of non-smooth oscillators, including an impact oscillator and a self-sustained friction oscillator. Time histories, bifurcation diagrams and Poincaré maps of the systems were determined experimentally and compared with numerical integration. Davis and Virgin [14] studied the simulated and experimental responses of a rigid-arm pendulum driven by an external impactor. A variety of qualitative responses of the system was observed through phase portrait, Poincaré maps, power spectra and bifurcation analysis. Batako, Lalor and Piiroinen [15] studied the dynamical behavior of a friction-driven vibro-impact system. To avoid the complexity of dealing with two discontinuous nonlinear forces (dry friction and impact), the dynamical response of the system without impact was investigated. The system equations of motion were solved numerically through a simulation method proposed by Piiroinen and Kuznetsov [16], which could be applied to piecewise smooth dynamical systems, particularly on systems with sliding motions.

This paper presents a numerical investigation into the dynamic responses of a new electro-vibro-impact system, which is suitable for ground moling application. The system is studied experimentally by Nguyen et al. [17]. Studies by Barkan [18] and Rodger et al. [19] revealed that vibro-impact systems produce a combination of vibration and impact and are able to achieve better soil penetration. The main aim of this paper is to identify the qualitative motion most suitable for the forward progression of the mechanism against resistive forces such as friction and soil resistance. Experimentation has identified period one motion and suitable operating frequencies [20]. However, for implementation in actual soil conditions, precise optimization would require a numerical tool to predict operating parameters at a minimal computational expense. More work may be done by a continuation of the theoretical work of Pavlovskaia et al. [3] and Wiercigroch et al. [4, 7, 21, 22] so as to finally achieve a real-time control strategy.

The new invention involves the use of a linear self-oscillation inductance motor of Mendrela [23, 24]. By placing a stop in the path of bar oscillations, impacts are generated. The electro-magnetic forces within the solenoid are dependent on the position of the bar, and function as nonlinear restoring forces. Hence, vibration of the mechanism is possible, which would be particularly useful in cohesionless soils. To address the issue of heat generated by the solenoid and metal bar, a solid state relay was used to switch a series RLC circuit on and off in accordance to a function generator [25]. Impact forces were substantially increased.

The establishment of a mathematical model in the present piece of work is an important milestone in the development of the electro-vibro-impact system. Deployment in the field would require an adaptive means of ensuring a constant forward velocity under varying soil conditions. One option would be to generate approximate analytical solutions to the mathematical equations of motion to complement a control strategy. In example of such an approach would be the treatment given to the impact oscillator by Woo et al. [26]. A systematic methodology of evaluating unknown coefficients numerically was presented. The modeling done here derived important ideas from Pavlovskaia et al. [27] and Wiercigroch [28]. By describing the frictional characteristics of the aluminium rails, analytical solutions may then be sought. Semi-analytical solutions have been sought for a similar system by Pavlovskaia and Wiercigroch [9], while maps have been derived by Pavlovskaia et al. [29]. Dimensional reduction for mapping has been treated in detail by Wiercigroch and Pavlovskaia [30]. With the present model, it is now possible to explore methods of classification, perhaps in the manner of Błażejczyk-Okolewska et al. [31]. Czolczynski and Kapitaniak [32] have recognized the direct influence on system response by the parameters, and the rich dynamical phenomenon, such as those observed by de Souza et al. [33] and Wiercigroch et al. [34] may be either exploited or avoided. Lenci and Rega [35] have presented an important approach to the analysis of an impact system, and their work in control [36] is an avenue to be explored in future work.

In this paper, the mathematical modeling of this new system is followed by numerical integration, using Dynamics [37] software. A variety of system responses are presented, indicating the practicality of the computational tool for optimization of the mechanism when deployed in soil conditions.

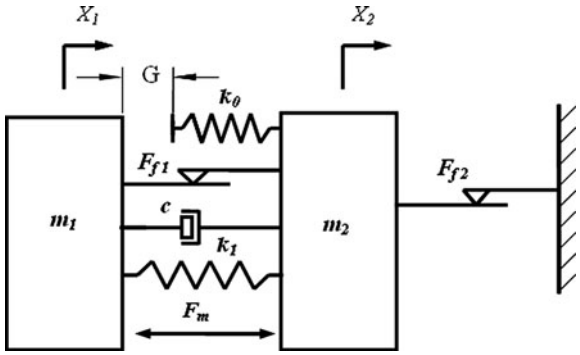

Fig. 1 Physical model of the mechanical part of the new vibro-impact system

2 Mathematical modeling

The physical model of the solenoid vibro-impact mechanism is shown in Fig. 1. The mechanical system is made up of two masses: the mass of the metal bar, m_1 and mass, m_2 corresponding to the total mass of the moving board and all remaining components placed on it. The relative motion of two masses, m_1, and m_2, generates nonlinear magnetic force inside the solenoid, F_m, linear viscous damping force, characterized by the damping coefficient c, and dry friction force, F_{f1}. The magnetic force is induced when the solid state relay switches the power on whereas the spring force of stiffness k_1 acts on both masses m_1 and m_2. Displacements of the bar, X_1 and of the board, X_2, are chosen as mechanical coordinates of the system. To model impacts of the metal bar upon the obstacle block, a spring of stiffness, k_0, is incorporated in the system. When the relative displacement of the bar with respect to the displacement of the board, X ($X = X_1 - X_2$), is greater than the clearance, G, the impact occurs. Finally a force, F_{f2}, models dry friction between the board and the rails.

Thus system can operate at the time in one of two different regimes listed below. The first regime occurs when the bar is not in contact with the obstacle block, i.e. $X_1 - X_2 < G$. The equations of motion for this regime are

$$\begin{aligned} m_1\ddot{X}_1 &= F_m - F_{f1} - c\big(\dot{X}_1 - \dot{X}_2\big) - F_{\text{spr}}, \\ m_2\ddot{X}_2 &= -F_m + F_{f1} + c\big(\dot{X}_1 - \dot{X}_2\big) + F_{\text{spr}} - F_{f2}, \end{aligned} \tag{1}$$

where dot denotes differentiation with respect to time, t. Once the relative displacement of the masses exceeds the clearance, $X_1 - X_2 \geq G$, the impact of the bar upon the block occurs and it is described as

$$\begin{aligned} m_1\ddot{X}_1 &= F_m - F_{f1} - c\big(\dot{X}_1 - \dot{X}_2\big) \\ &\quad - F_{\text{spr}} - k_0(X_1 - X_2 - G), \\ m_2\ddot{X}_2 &= -F_m + F_{f1} + c\big(\dot{X}_1 - \dot{X}_2\big) + F_{\text{spr}} \\ &\quad + k_0(X_1 - X_2 - G) - F_{f2}. \end{aligned} \tag{2}$$

Here, the dry friction forces F_{f1} and F_{f2} are calculated as

$$\begin{aligned} F_{f1} &= \mu_1 m_1 g\,\text{sgn}\big(\dot{X}_1 - \dot{X}_2\big), \\ F_{f2} &= \mu_1(m_1 + m_2)g\,\text{sgn}\big(\dot{X}_2\big), \end{aligned} \tag{3}$$

where μ_1 and μ_2 are appropriate frictional coefficients and g is the acceleration due to gravity.

The restoring force, F_{spr}, of the additional spring is calculated as

$$F_{\text{spr}} = k_1(X_1 - X_2 - X_0), \tag{4}$$

where X_0 is the equilibrium position of the additional coil spring when it is uncompressed.

The coupling between the mechanical system and electrical circuit is described by a nonlinear magnetic force, F_m, which is generated in the solenoid and depends on the characteristics of the electrical circuits, as will be explained.

The equation describing the electric circuit dynamics can be expressed as

$$\frac{d\psi}{dt} + Ri + \frac{1}{C}\int i\,dt = V(t), \tag{5}$$

where ψ is the magnetic flux in the solenoid and $\psi = Li$, L is the solenoid inductance, i is the current, R is the resistance, C is the capacitance, and $V(t)$ is the externally supplied time dependent voltage. As the solenoid has the movable core (metal bar oscillating inside the solenoid), its inductance depends on the relative displacement between the bar and the board,

$$L = L\big(X_1(t) - X_2(t)\big). \tag{6}$$

Thus, introducing notation for the relative displacement, $X = X_1 - X_2$, we have $L = L(X)$, and

$$\frac{d\psi}{dt} = i\frac{\partial L}{\partial x}\big(\dot{X}_1 - \dot{X}_2\big) + L\frac{di}{dt}. \tag{7}$$

Substituting (7) into (5) we have

$$i\frac{\partial L}{\partial x}\big(\dot{X}_1 - \dot{X}_2\big) + L\frac{di}{dt} + Ri + \frac{1}{C}\int i\,dt = V(t). \tag{8}$$

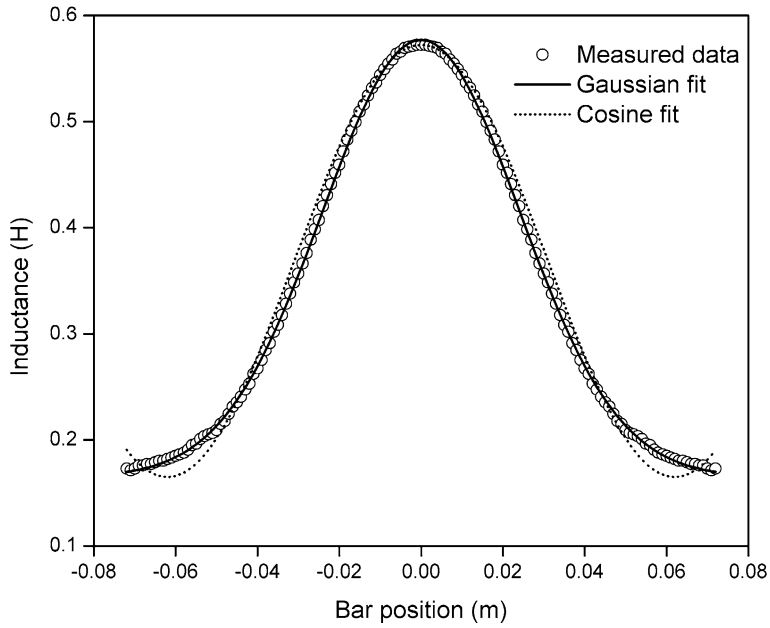

Fig. 2 Variation of the inductance of the solenoid approximated by a Gaussian and cosine fit

Finally, differentiating (7) with respect to time to eliminate an integral, the equation of the circuit is obtained as

$$L\frac{d^2i}{dt^2}+\left[R+2\frac{\partial L}{\partial X}\left(\dot{X}_1-\dot{X}_2\right)\right]\frac{di}{dt} +\left[\frac{1}{C}+\frac{\partial^2 L}{\partial X^2}\left(\dot{X}_1-\dot{X}_2\right)^2+\frac{\partial L}{\partial X}\frac{d^2X}{dt^2}\right]i =\frac{dV(t)}{dt}. \tag{9}$$

In this equation describing the current, the dependence of the inductance of the coils on the relative displacement (the unknown function $L(X)$) is adopted in a Gaussian form

$$L(X)=L_0+\frac{A}{\sigma\sqrt{\pi/2}}e^{-2(X/\sigma)^2}, \tag{10}$$

where L_0 is the inductance of the solenoid without the bar, A is a coefficient of the function, e is the base of natural logarithm and σ is a standard deviation.

A reference form of the inductance of a solenoid is the one made by Mendrela [23, 24]

$$L(X)=\frac{L_{\max}-L_{\min}}{2}\left[1+\cos\left(\frac{\pi X}{\lambda}\right)\right]+L_{\min}, \tag{11}$$

where $L_{\max}$ is inductance of the solenoid with the metal bar placed in the center of the coil, $L_{\min}$ is inductance of the solenoid without the bar, and λ is the length of the solenoid.

It has been found that the Gaussian form is fitted measured inductance data better than the cosine form, as can be seen in Fig. 2. Consequently, the Gaussian form of the inductance is used in this study.

Externally supplied voltage has been chosen as a typical sinusoidal form, $V(t)=V_s\sin(\Omega t)$, where V_s is the voltage amplitude and Ω is the frequency of power supply. Hence, the right side of (9) can be rewritten as

$$\frac{dV(t)}{dt}=\Omega V_s\cos(\Omega t). \tag{12}$$

Using a solid state relay, the power supplying the solenoid is switched on and off periodically with a frequency of F_{ctr}. Consequently, a factor, P_{ctr}, reflecting the voltage variation is used and (9) can be rewritten in the form

$$L\frac{d^2i}{dt^2}+\left[R+2\frac{\partial L}{\partial X}\left(\dot{X}_1-\dot{X}_2\right)\right]\frac{di}{dt} +\left[\frac{1}{C}+\frac{\partial^2 L}{\partial X^2}\left(\dot{X}_1-\dot{X}_2\right)^2+\frac{\partial L}{\partial X}\frac{d^2X}{dt^2}\right]i =\Omega P_{\text{ctr}}V_s\cos(\Omega t). \tag{13}$$

The factor of control frequency, P_{ctr}, can be expressed as following. Since the control signal is a rectangular waveform with a frequency of F_{ctr} and the

solid state relay will switch the power on when the signal is positive, the variation of P_{ctr} can be represented in the form

$$P_{\text{ctr}} = \begin{cases} 1, & \text{if } t\left(\text{mod}\frac{1}{F_{\text{ctr}}}\right) < \frac{1}{2F_{\text{ctr}}}, \\ 0, & \text{otherwise}, \end{cases} \tag{14}$$

where P_{ctr} is a dimensionless term and F_{ctr} has the unit of Hz. Substituting $\frac{dX}{dt} = \dot{X}_1 - \dot{X}_2$ into (13) we obtain

$$\begin{aligned} &L\frac{d^2i}{dt^2} + \left[R + 2\frac{\partial L}{\partial X}\frac{dX}{dt}\right]\frac{di}{dt} \\ &\quad + \left[\frac{1}{C} + \frac{\partial^2 L}{\partial X^2}\left(\frac{dX}{dt}\right)^2 + \frac{\partial L}{\partial X}\frac{d^2X}{dt^2}\right]i \\ &= \Omega V_s \cos(\Omega t). \end{aligned} \tag{15}$$

To complete the mathematical description of the system, a nonlinear magnetic force, F_m, has to be defined. From an energy conservation principle [38], the equation describing the magnetic force in the solenoid with the movable core can be derived considering the stored magnetic energy inside the solenoid as

$$F_m = \frac{1}{2}i^2\frac{\partial L}{\partial X}. \tag{16}$$

Thus the coupled equations of the system are finally derived in the form

$$\begin{aligned} m_1\ddot{X}_1 &= \frac{1}{2}i^2\frac{\partial L}{\partial X} - \mu_1 m_1 g\,\text{sgn}\left(\dot{X}_1 - \dot{X}_2\right) \\ &\quad - c\left(\dot{X}_1 - \dot{X}_2\right) - k_1(X_1 - X_2 - X_0) \\ &\quad - k_0(X_1 - X_2 - G)H(X_1 - X_2 - G), \\ m_2\ddot{X}_2 &= -\frac{1}{2}i^2\frac{\partial L}{\partial X} + \mu_1 m_1 g\,\text{sgn}\left(\dot{X}_1 - \dot{X}_2\right) \\ &\quad + c\left(\dot{X}_1 - \dot{X}_2\right) + k_1(X_1 - X_2 - X_0) \\ &\quad + k_0(X_1 - X_2 - G)H(X_1 - X_2 - G) \\ &\quad - \mu_2(m_1 + m_2)g\,\text{sgn}\left(\dot{X}_2\right), \\ L\frac{d^2i}{dt^2} &+ \left[R + 2\frac{\partial L}{\partial X}\frac{dX}{dt}\right]\frac{di}{dt} \\ &\quad + \left[\frac{1}{C} + \frac{\partial^2 L}{\partial X^2}\left(\frac{dX}{dt}\right)^2 + \frac{\partial L}{\partial X}\frac{d^2X}{dt^2}\right]i \\ &= \Omega P_{\text{ctr}} V_s \cos(\Omega t), \end{aligned} \tag{17}$$

where $H(.)$ is Heaviside step function defined as

$$H(x) = \begin{cases} 1, & \text{if } x > 0 \\ 0, & \text{if } x \le 0, \end{cases} \tag{18}$$

and the function $L(X)$ is described by (10).

3 Simulation

Equations (17) have been rewritten as a system of first order differential equations and then solved using Dynamics software [37]. The obtained results are compared with experimental results.

In the case of impact, both X_1 and X_2 will gradually increase over time (since the moling machine will progress forward). In order to facilitate the study of bifurcation and phase plane analysis, relative displacement and relative velocity of X_1 and X_2 were chosen as two of the variables.

Let u and v be the relative displacement and relative velocity of the metal bar and the moling machine respectively, where

$$\begin{aligned} u &= X_1 - X_2, \\ v &= \dot{X}_1 - \dot{X}_2. \end{aligned} \tag{19}$$

Equations (17) can be rewritten as a system of first order ordinary differential equations as follow:

$$\begin{aligned} u' &= v, \\ v' &= \left(\frac{1}{m_1} + \frac{1}{m_2}\right)\left[\frac{1}{2}y^2\frac{\partial L}{\partial u} - \mu_1 m_1 g\,\text{sgn}(v)\right. \\ &\quad \left. - k_0(u - G)H(u - G) - cv - k_1(u - X_0)\right], \\ w' &= x, \\ x' &= \frac{1}{m_2}\left[-\frac{1}{2}y^2\frac{\partial L}{\partial u} + \mu_1 m_1 g\,\text{sgn}(v)\right. \\ &\quad + k_0(u - G)H(u - G) + cv \\ &\quad \left. + k_1(u - X_0) - \mu_2(m_1 + m_2)g\,\text{sgn}(x)\right], \\ y' &= z, \\ z' &= \frac{1}{L}\left[\Omega P_{\text{ctr}} V_s \cos(\Omega t) - \left(R + 2\frac{\partial L}{\partial u}v\right)z\right. \\ &\quad \left. = \left(\frac{1}{C} + \frac{\partial^2 L}{\partial u^2}v^2 + \frac{\partial L}{\partial u}v'\right)y\right]. \end{aligned} \tag{20}$$

The state variables are

u relative displacement of the metal bar with respect to the mole
v relative velocity of the metal bar with respect to the mole
w displacement of the mole
x velocity of the mole
y current, and
z first derivative of the current.

The experimental results were obtained with set of parameters as following.

First parameters of the RLC circuit and, in particular, the solenoid were identified. The minimal inductance, L_0, was measured as 0.1658 H, and the resistance of the solenoid was measured as $R = 27.5\ \Omega$. The inductance of the solenoid was measured and then fitted to the Gaussian form of (10) with the coefficient $A = 0.02494$ and the standard deviation $\sigma = 0.0483$.

The mass of the metal bar oscillating inside the solenoid was measured as 0.297 kg, whereas the total weight of the board with all components placed on it excluding the metal bar is 2.94 kg. The gap between the solenoid and the stop was maintained at -2 mm. This distance was experimentally found to be suitable for generation of the bar oscillations which caused substantial impacts. The stiffness of the additional spring was measured as $k_1 = 200$ N/m. The balance position of the support spring was set to be $X_0 = -22$ mm.

The impact stiffness can be estimated from the experimental results by using the principle of work done and energy. The total work done on the metal bar by the magnetic force and the frictional force when it moves from the position just before the impact, denoted as x_{10}, to the position where the stop has the maximum compression (i.e. $X_1 - X_2 - G$ is maximum), denoted as x_{11}, is equivalent to the change in the kinetic energy of the metal bar, the change in the potential energy stored in the spring and the change in the potential energy stored in the stop. The equation is as follows:

$$\int_{x_{10}}^{x_{11}} F_m\, d(X_1) + \int_{x_{10}}^{x_{11}} F_{f1}\, d(X_1) = \frac{1}{2} m_1 \left(\dot{x}_{11}^2 - \dot{x}_{10}^2\right) + \frac{1}{2} k_1 \left(x_{11}^2 - x_{10}^2\right) + \frac{1}{2} k_0 \left(x_{11}^2 - x_{10}^2\right). \tag{21}$$

However, due to the very small compression of the stop, work done by the magnetic force and the frictional force in that interval is small compared to the change in the kinetic energy of the metal bar and the potential energy stored in the stop. The change in the spring potential energy is also small since k_1 is estimated to be 200 N/m only. Therefore the impact stiffness can be estimated by the following expression:

$$k_0 = \frac{m_1(\dot{x}_{10}^2 - \dot{x}_{11}^2)}{x_{11}^2 - x_{10}^2}. \tag{22}$$

The velocity of the metal bar at the position x_{10} was estimated by calculating the derivative of 5 consecutive linear variable displacement transducer (LVDT) data points and the averaged value was used. The velocity of the metal bar at the position x_{11} was taken as zero. The impact stiffness was then estimated to be 1.24×10^5 N/m.

The simulation results were obtained by using the parameter values as the same as in experiments. In addition, the frictional coefficient between the bar and the solenoid μ_1 was approximately measured when the bar was oscillating at the applied root-mean-square (RMS) voltage of 58 V ($V_s = \sqrt{2} V_{\text{rms}} = 82.02$ V) and the capacitance in the circuit equal to 32 μF. It was then adjusted to match the experimental result in the same condition, so it was finally determined as $\mu_1 = 0.295$. The frictional coefficients between the board and the rails was found to be approximately $\mu_2 = 0.235$. It was determined using a force consideration on the board which was moving slowly at constant speed. To achieve such slow motion one end of a string was attached to the board while a certain weight was fixed on its other end hanging over the experimental table and causing the rig to move forward. In this case the frictional force acting on the board was balanced by the tension force in the string dependent on the hanging weight and thus allowing for the estimation of the friction coefficient. Finally, in the numerical model, the dissipation coefficient is set at $c = 0.155$ kg/s.

A comparison was made between experimental data and predictions made with the new mathematical model. For a function generator signal of 2.5 Hz, 3 Hz, 5 Hz, 7 Hz, 8 Hz, 9 Hz and 13 Hz, time histories were plotted in the first instance. To further confirm the topology, phase planes of the steady-state motion were constructed. The equations of motion were nu-

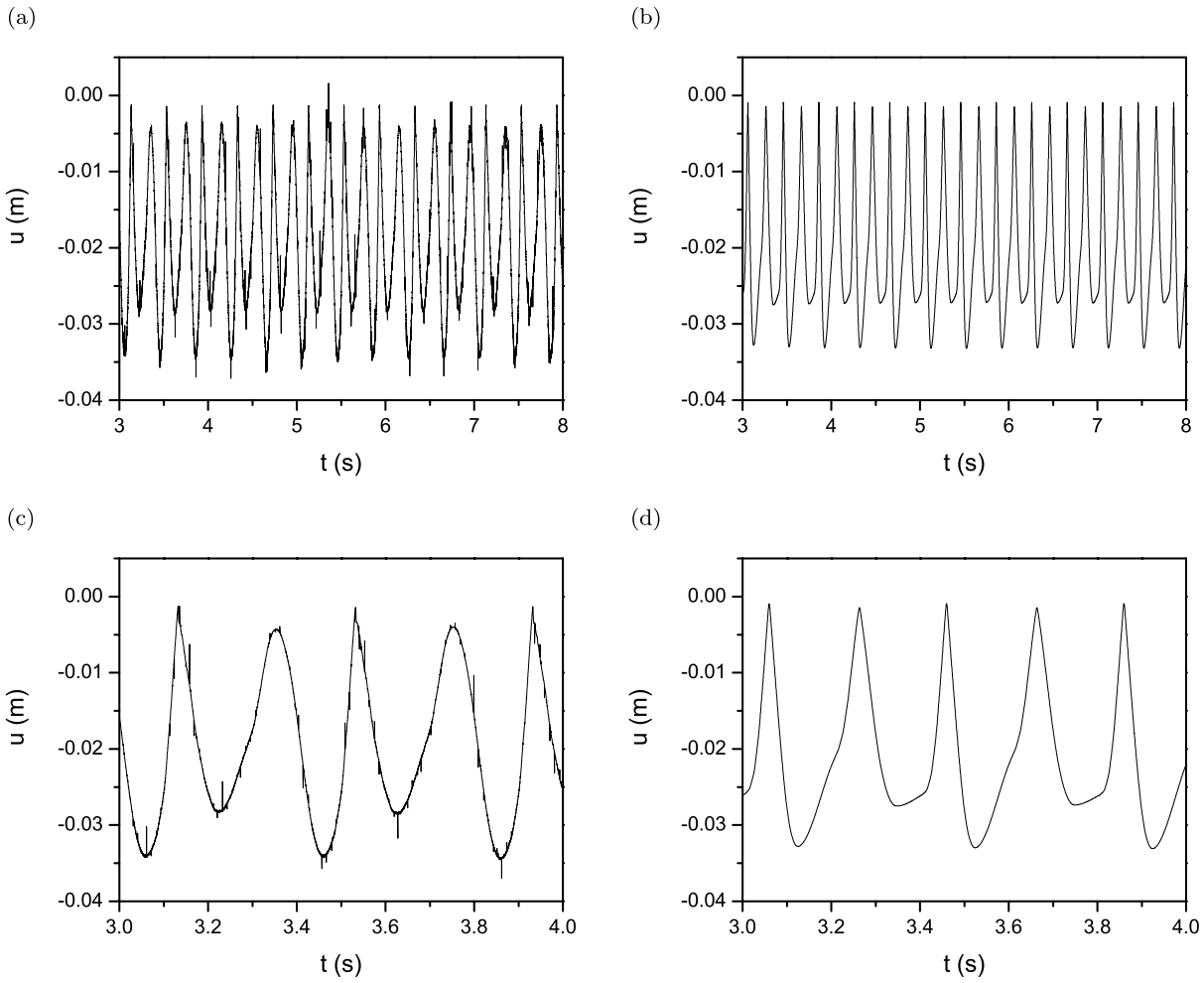

Fig. 3 Relative displacement-time history of the metal bar for a frequency of the control signal of 5 Hz obtained from (**a**) experiment, (**b**) numerical integration, (**c**) 1 second of the experiment and (**d**) 1 second of the numerical integration

merically integrated with Dynamics [37] software to scrutinize the time histories. Prior to this, it had already been experimentally observed that there was a range of working frequencies within which the forward progression was the fastest. When the supplied RMS voltage was 58 V, typically, the frequencies were slightly less than 10 Hz. For frequencies of 5 Hz, 7 Hz and 8 Hz, the qualitative dynamics have been captured by the model. In Fig. 3(a), the amplitude of the motion alternates between two values in the laboratory. This response has been numerically predicted in Fig. 3(b). The similarity in the amplitudes has been achieved by setting the damping coefficient, c, to a value of 0.155 kg/s. This has been the same value used in numerical predictions, to ensure consistency. By inspecting a shorter range of time from the third to the fourth second, the numerical computation of Fig. 3(d) shows a close correlation to the amplitude variation of Fig. 3(c). Small vertical spikes observed in Fig. 3(c), contributed by laboratory noise, are not found in Fig. 3(d). Half of the experimental waveform is rounded at a local maxima. However, this has not been forecast by the mathematical model. The local minima have also been flattened. For this set of parameter values, the qualitative dynamics have been accurately portrayed, and quantitative amplitudes have also been well-described. Detail pertaining to the shape of the waveform still need to be portrayed. This may be achieved with further refinement of the model.

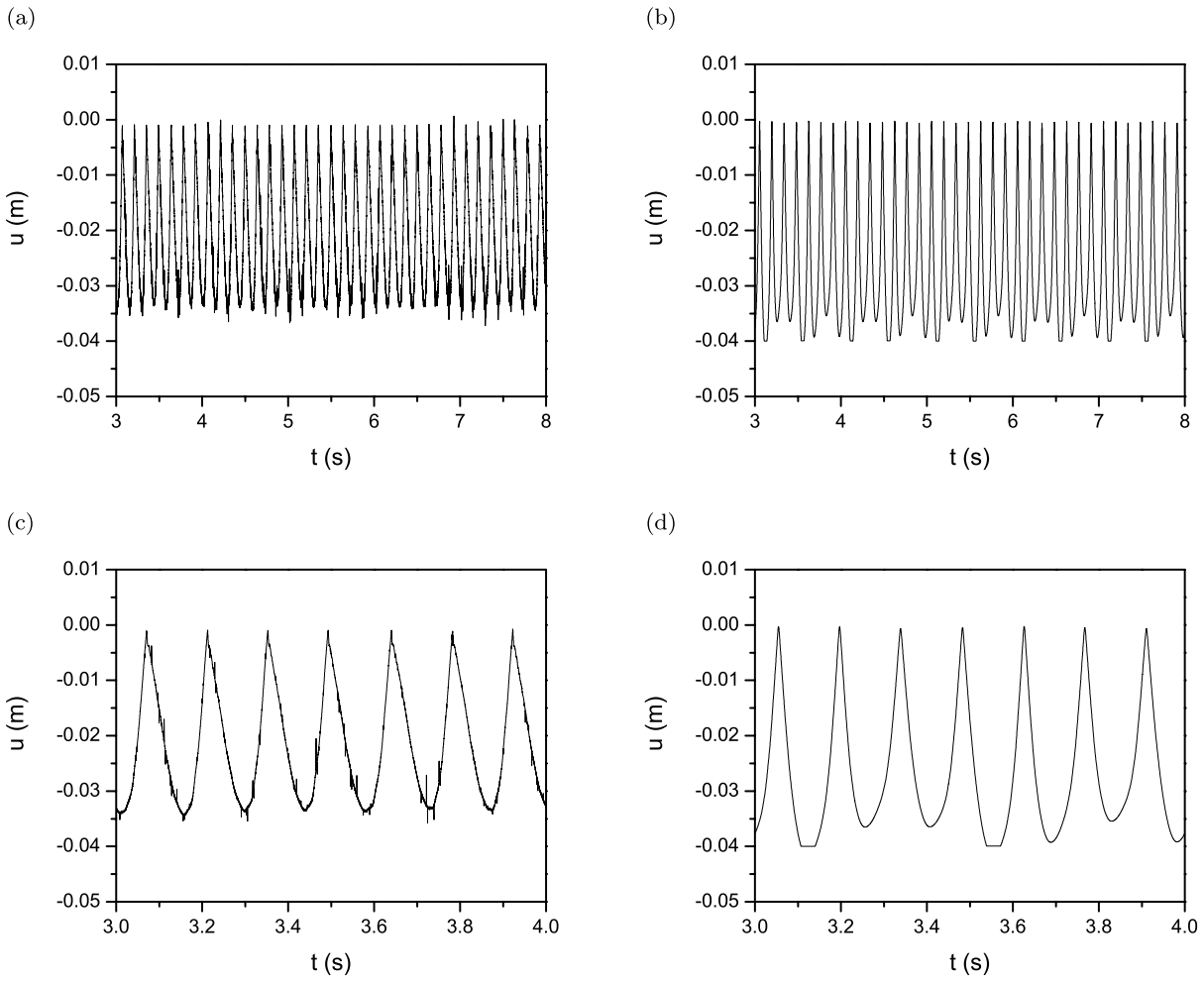

Fig. 4 Relative displacement-time history of the metal bar for a frequency of the control signal of 7 Hz obtained from (**a**) experiment, (**b**) numerical integration, (**c**) 1 second of the experiment and (**d**) 1 second of the numerical integration

On increasing the frequency to 7 Hz, a periodic motion is observed in Fig. 4(a). The amplitude of motion is nearly the same. However, it varies in such a way that it would increase, and then decrease, before repeating itself again. This phenomenon has also been illustrated by the mathematical model in Fig. 4(b). The amplitude of bar oscillations, however, exhibit more variation and a larger minimum amplitude. The discrepancy in amplitude is highlighted in Fig. 4(c) and (d). The frequency of 8 Hz is close to an optimum operating frequency, as reported by Nguyen and Woo [25]. A synchronous periodic motion is noted in Fig. 5(c). The steady-state solution to the mathematical model describes this quite well in Fig. 5(d). On a longer time-scale, both Fig. 5(a) and (b) illustrate a small variation in amplitude, especially the former. This change about a mean value might have been caused by additional friction induced by the linear variable displacement transducer (LVDT). Other sources of variable frictional characteristics are the rough surface of laminated metal bar.

The irregular motion, suggestive of chaos, had been observed in the laboratory for lower frequencies. For example, at a frequency of 2.5 Hz, an interesting waveform is shown in Fig. 6(a). The haphazard nature of this response has the following characteristics: it drops to smaller amplitudes at irregular instants in time, and indicates higher harmonics during these smaller amplitudes. Figure 6(b) simulates the trajectory for the

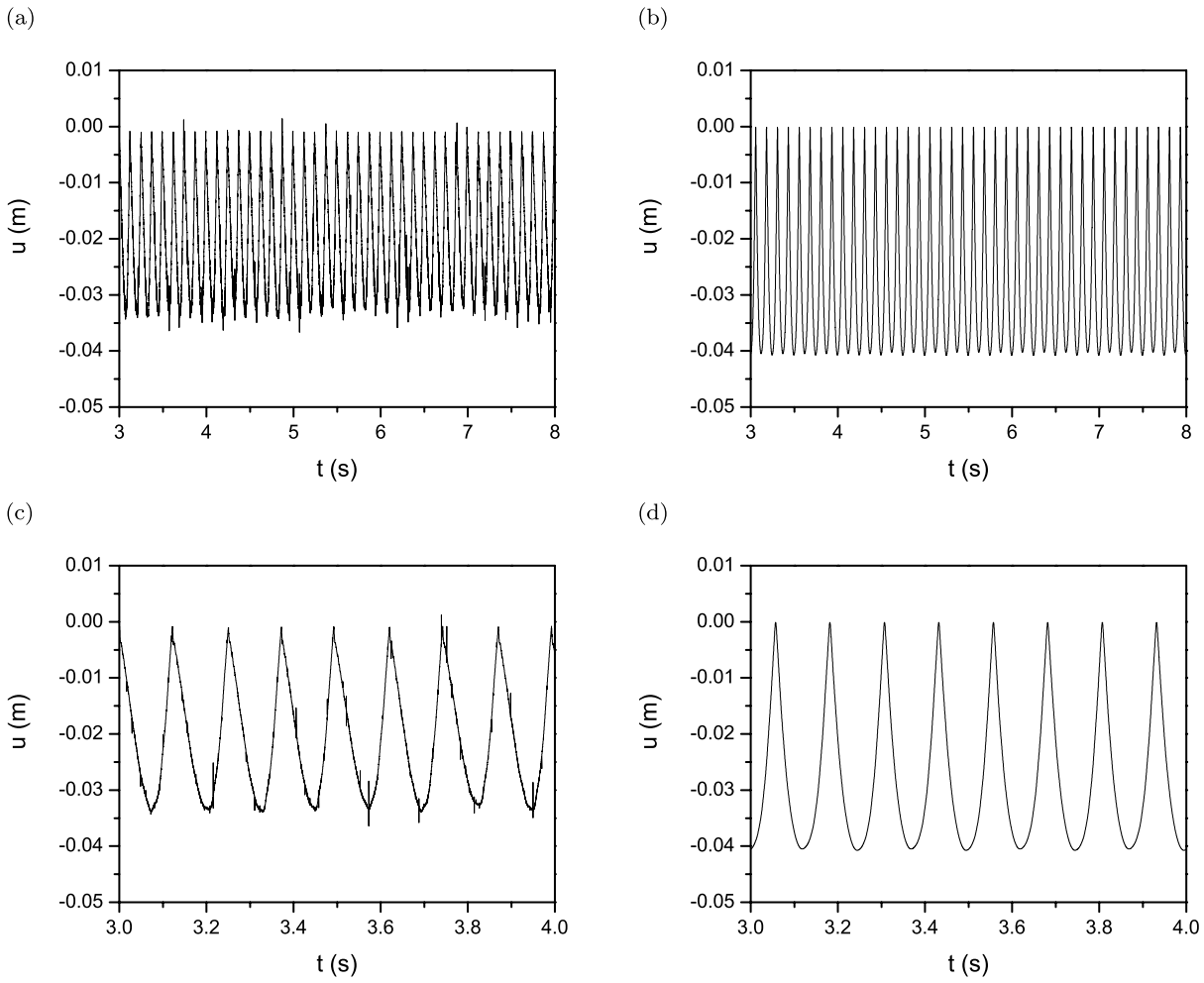

Fig. 5 Relative displacement-time history of the metal bar for a frequency of the control signal of 8 Hz obtained from (**a**) experiment, (**b**) numerical integration, (**c**) 1 second of the experiment and (**d**) 1 second of the numerical integration

same set of system parameter values. Some of the irregularity in motion is replicated. However, there is discrepancy in the order of variation of the amplitude. The similarities and differences are shown in greater detail in Fig. 6(c) and (d). From the third second to the fourth second, two maxima are shown, before plunging to a local minimum value, which increases to achieve two successive maxima, before decreasing again. In Fig. 6(d), these fluctuations have been predicted. However, the first two local maxima are sharper than observed in practice, and the next successive maxima are different in amplitude when compared to each other. The minimum value is accurate, although predicted to occur before it actually happens. The numerical computation in Fig. 6(d) also shows an additional lag in time at 3.6 s, which does not exist in the laboratory.

The main shortcoming of the current model is that it is not yet able to accurately predict the amplitudes of the system response at frequencies higher than the optimum value. Figure 7(a) displays the relative motion of the bar when the function generator is set at 9 Hz. A waveform which is quite regular is depicted, which is punctuated by short intervals of small displacement amplitudes. On closer inspection of this waveform in 1 second in Fig. 7(c), the larger amplitudes are similar in magnitude. The numerical integration of Fig. 7(b) yields a smaller amplitude of approximately 0.005 m, as compared to 0.03 m seen in experiment. This difference is seen more clearly in Fig. 7(c) and (d).

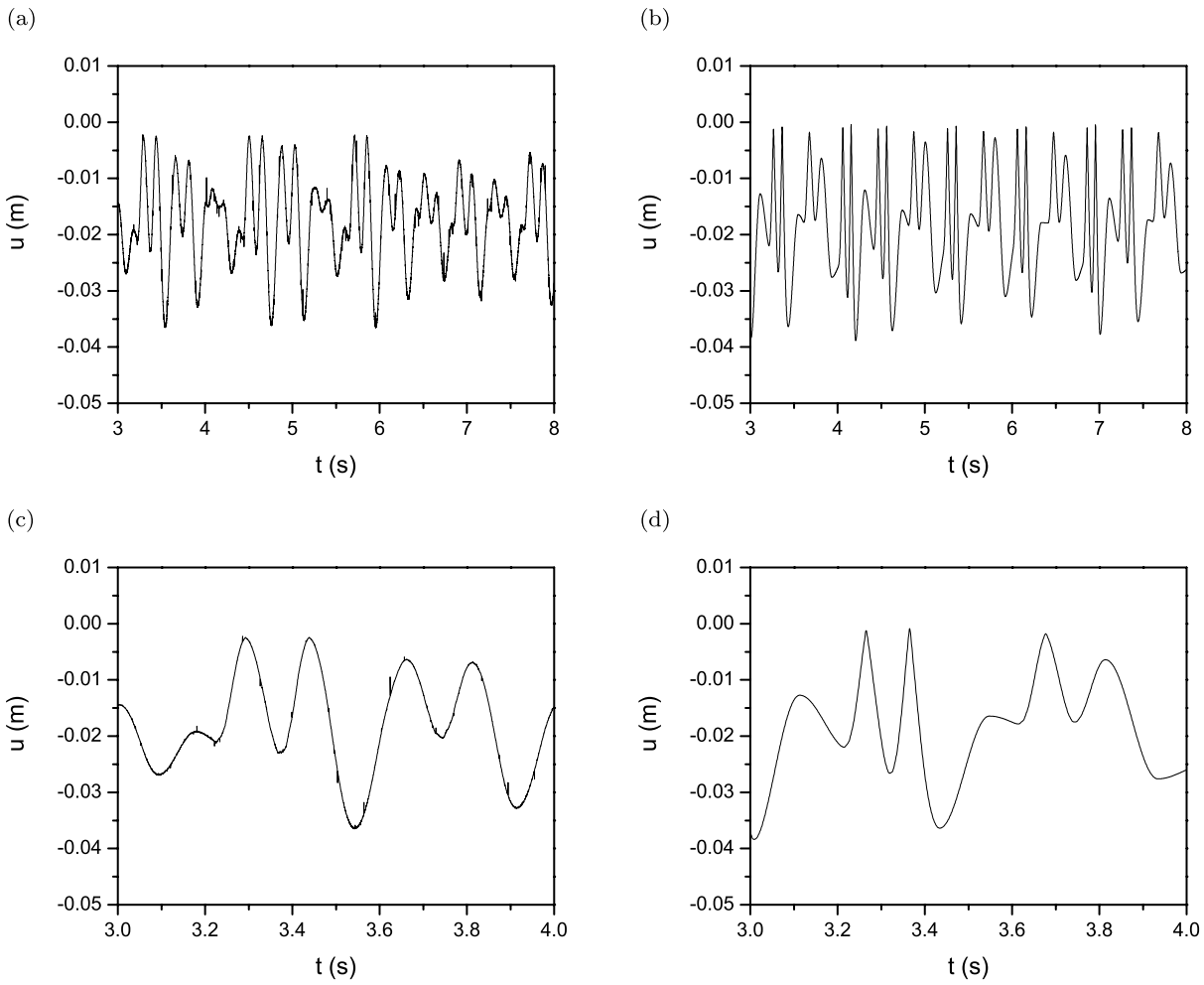

Fig. 6 Relative displacement-time history of the metal bar for a frequency of the control signal of 2.5 Hz obtained from (**a**) experiment, (**b**) numerical integration, (**c**) 1 second of the experiment and (**d**) 1 second of the numerical integration

Phase planes of the steady-state motion were constructed alongside Poincaré maps to confirm the nature of the orbit. The irregular motion detected at lower frequencies has been found to exist within an attractor of chaotic motion. From the time history of Fig. 6, the chaos is shown again in Fig. 8(a) where there is no clear indication of any periodic orbit. The first 12 cycles of motion were taken to be transient and not included so as to plot the steady state. By sampling data points at the same frequency, a closed form of the attractor is seen in Fig. 8(b). Computation of a maximum Lyapunov exponent via LyapOde (a "C" routine [39] written based on QR decomposition method [40]) for this frequency has yielded a value of 6.67, which provided further evidence of a chaotic trajectory. Another piece of evidence of a transition from chaotic motion to periodic motion is the construction of a bifurcation diagram, which was analyzed experimentally in [25] and numerically in [41].

However, chaotic motion predicted at a higher frequency may also be more simply found to linger within a definite range of displacement and velocity as shown in Fig. 9.

Previous work had identified periodic motion to be most beneficial to the soil penetration progress. The mathematical model is capable of locating such attractors [41]. Both period-1 and period-2 orbits have been computed.

To further confirm the qualitative nature of the dynamics responses, a basin of attraction was plotted for

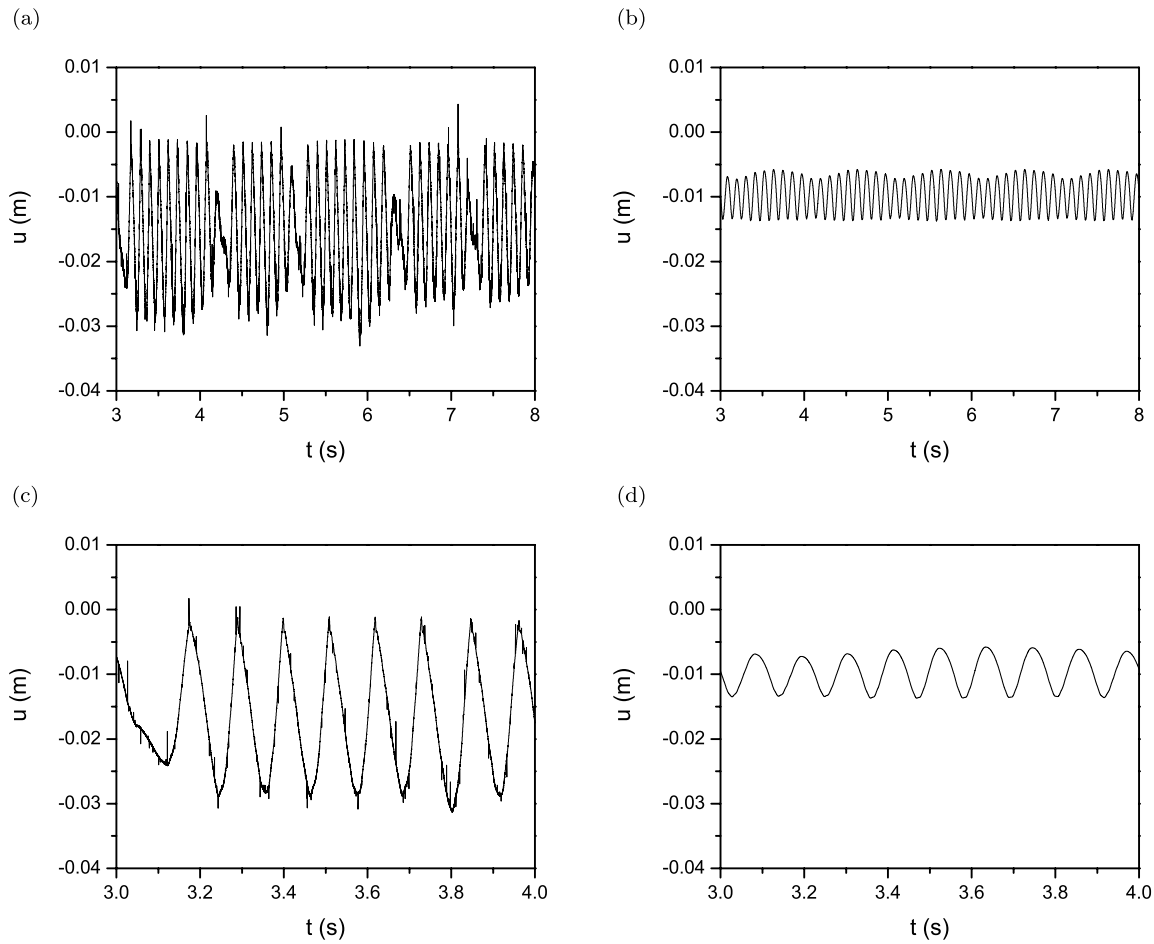

Fig. 7 Relative displacement-time history of the metal bar for a frequency of the control signal of 9 Hz obtained from (**a**) experiment, (**b**) numerical integration, (**c**) 1 second of the experiment and (**d**) 1 second of the numerical integration

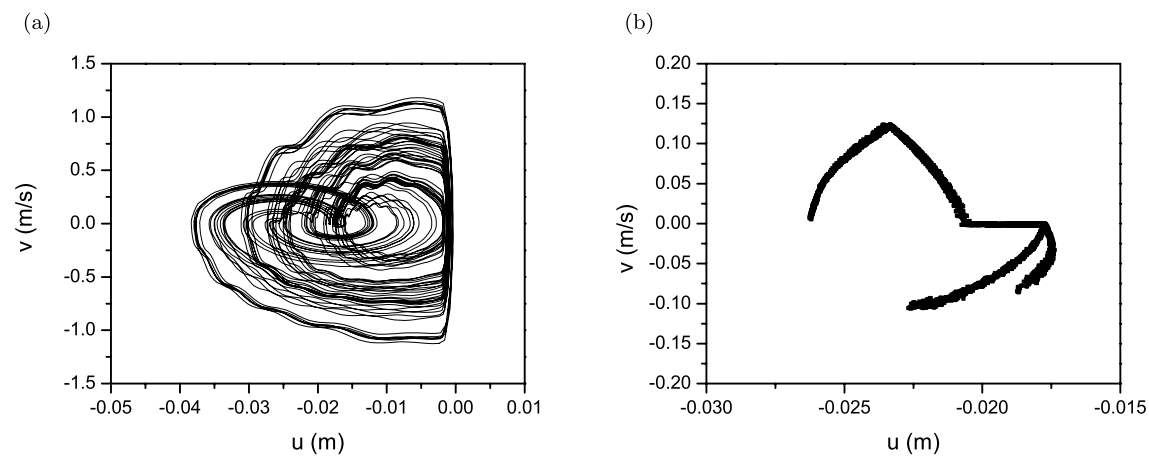

Fig. 8 (**a**) Phase plane and (**b**) Poincaré map of motion of bar relative to the base plate at a control frequency of 2.5 Hz

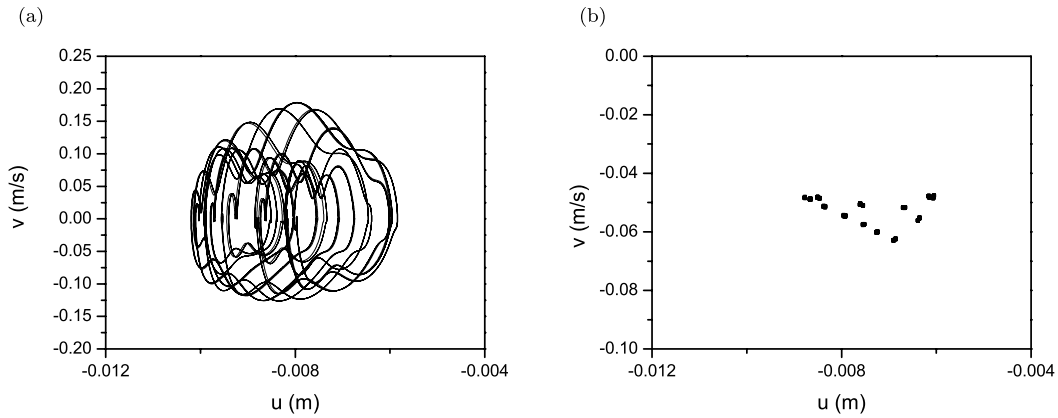

Fig. 9 (**a**) Phase plane and (**b**) Poincaré map of motion of bar relative to the base plate at a control frequency of 13 Hz. The first 65 cycles of motion were taken to be transient

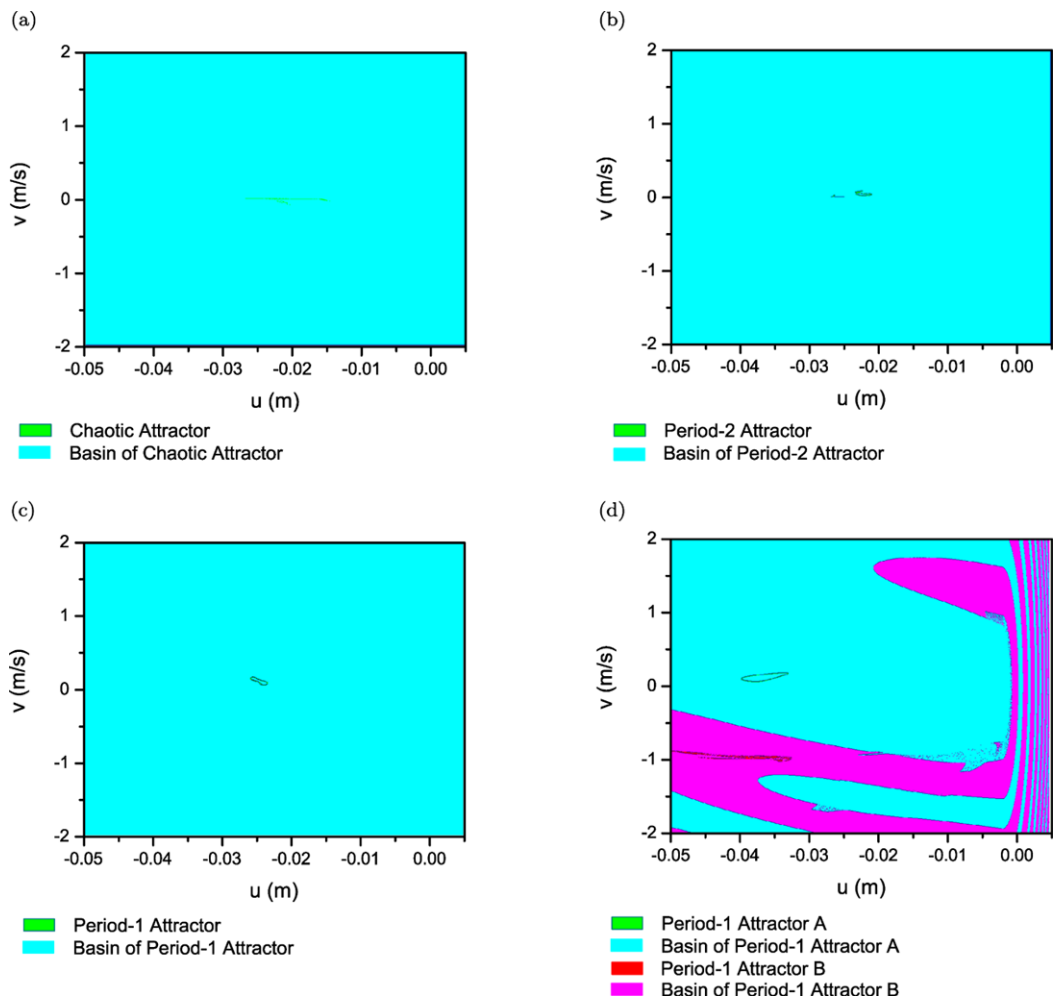

Fig. 10 Basin of attraction numerically constructed for the same system parameters as in [25]. The set of initial conditions ranges from −0.05 m to 0.005 m for relative displacement and −2 m/s to 2 m/s for the relative velocity. The control frequency ranges from (**a**) 29.5 rad/s (4.695 Hz); (**b**) 31 rad/s (4.93 Hz); (**c**) 32.8 rad/s (5.22 Hz) and (**d**) 47 rad/s (7.48 Hz)

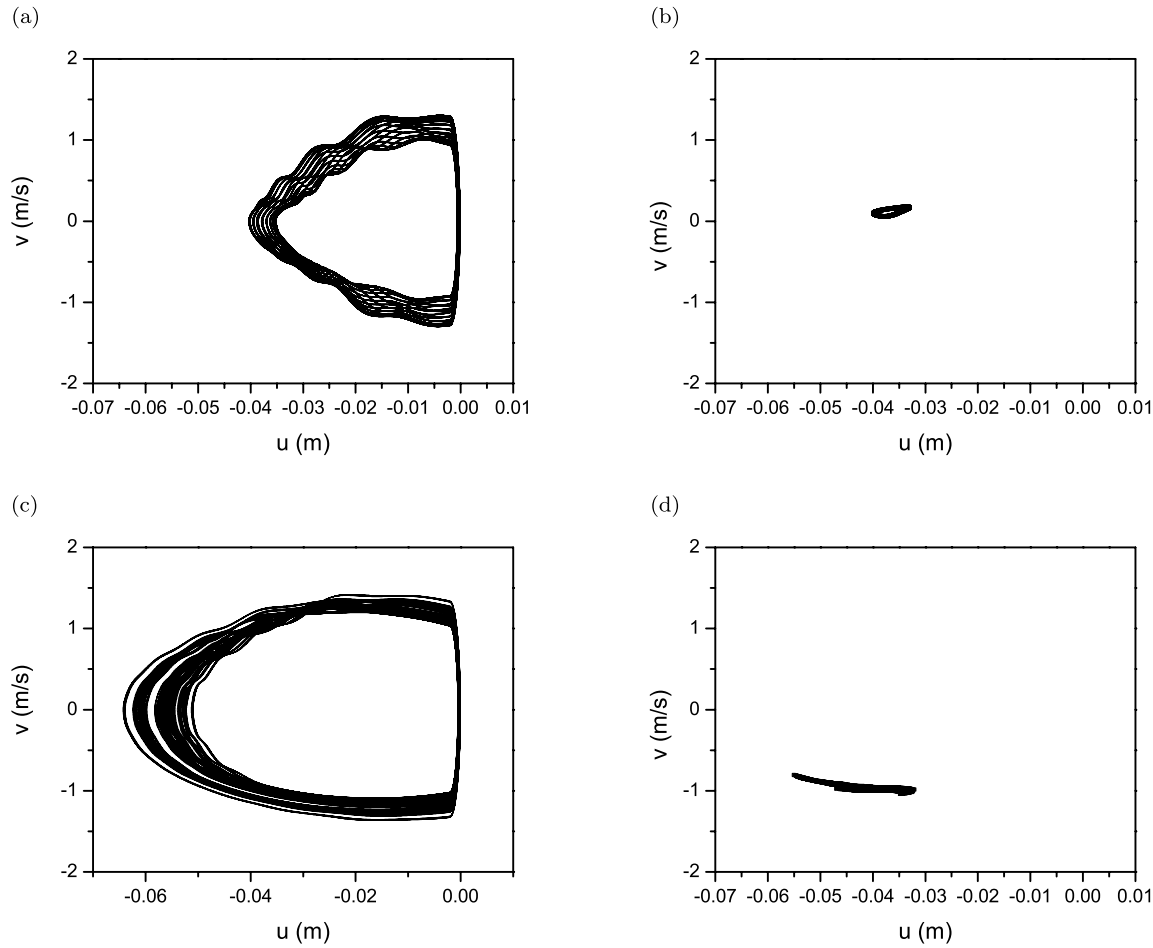

Fig. 11 Phase planes and Poincaré maps of motion of bar relative to the base plate at a control frequency of 47 rad/s (7.48 Hz) based on two sets of initial conditions: (**a**) phase plane and (**b**) Poincaré map of initial relative displacement of -0.022 m and relative velocity of 0 m/s (corresponding to the cyan basin in Fig. 10(d)); (**c**) phase plane and (**d**) Poincaré map of initial relative displacement of -0.045 m and relative velocity of -1 m/s (corresponding to the magenta basin in Fig. 10(d))

the same set of parameter values. A set of initial conditions of -0.05 m to 0.005 m for the relative displacement and -2 m/s to 2 m/s for the relative velocity was selected to mimic experimental conditions. There is only one attractor shown in the basin of attraction for the control frequency of 29.5 rad/s (4.695 Hz), 31 rad/s (4.93 Hz) and 32.8 rad/s (5.22 Hz). The attractor appears to be chaotic when the control frequency is 29.5 rad/s (4.695 Hz). As the control frequency increases to 31 rad/s (4.93 Hz), the attractor is period-2 in nature, represented by the 2 green dots in Fig. 10(b). When the control frequency changes to 32.8 rad/s (5.22 Hz), the attractor becomes a small circle as shown in Fig. 10(c), settling to a period-1 attractor. The attractor is a circle instead of a point due to the fact that the phase portrait actually fluctuates within a small area. On increasing the control frequency to 47 rad/s (7.48 Hz), two attractors appear in the basin of attraction. These two attractors, one in green circle while the other one in a thin red loop, are period-1. This is double confirmed by drawing the phase diagram using two sets of initial conditions, one for each basin. The phase plane diagram is shown in Fig. 11. It shows that both attractors have a single period. The Poincaré maps further confirmed the shape of the two attractors shown in Fig. 10(d). The first 37 cycles of motion (for approximately 5 seconds) were taken to be transient and not included in the diagram.

4 Conclusions

By scrutinising the system responses of the new electro-vibro-impact system, it has been found that both periodic and chaotic trajectories exist. Mathematical modeling has established a correlation with experimental data, and hence can be used as a numerical tool to optimize the mechanism when it is deployed in actual soil conditions. Of the important parameters to which the machine performance is sensitive, attention has been paid to the variation in the control frequency. The progression rate and impact force of the machine have been found to be largest when periodic trajectories of the metal bar exist. Time histories demonstrate a wide variety of responses, from period one, period two to chaotic. Poincaré maps have also been constructed to identify the attractors. The qualitative response has been verified with basins of attraction.

On gaining more confidence in this mathematical model, future endeavors to optimize and control the system would be able to start with a set of equations. In this way, either approximate or exact analytical solutions may be sought for future experimental verification.

Acknowledgements The authors would like to express their thanks to the Vietnamese Government for financial support to V.-D. Nguyen. They are also grateful to the University of Nottingham Malaysia Campus for the funding of J.-H. Ho.

References

1. Wiercigroch, M.: Applied nonlinear dynamics of non-smooth mechanical systems. J. Braz. Soc. Mech. Sci. Eng. **28**(4), 521–528 (2006)
2. Shaw, S.W., Holmes, P.J.: A periodically forced piecewise linear oscillator. J. Sound Vib. **90**(1), 129–155 (1983)
3. Pavlovskaia, E., Wiercigroch, M., Grebogi, C.: Modelling of an impact system with a drift. Phys. Rev. E **64**, 056224 (2001) (9 pages)
4. Wiercigroch, M., Sin, V.T.W.: Experimental study of base excited symmetrically piecewise linear oscillator. ASME J. Appl. Mech. **65**(3), 657–663 (1998)
5. Peterka, F., Vacik, J.: Transition to chaotic motion in mechanical systems with impacts. J. Sound Vib. **154**(1), 95–115 (1992)
6. Peterka, F.: Bifurcations and transition phenomena in an impact oscillator. Chaos Solitons Fractals **7**(10), 1635–1647 (1996)
7. Wiercigroch, M.: Modelling of dynamical systems with motion dependent discontinuities. Chaos Solitons Fractals **11**(15), 2429–2442 (2000)
8. Pavlovskaia, E., Wiercigroch, M.: Analytical drift reconstruction for visco-elastic impact oscillators operating in periodic and chaotic regimes. Chaos Solitons Fractals **19**(1), 151–161 (2004)
9. Pavlovskaia, E., Wiercigroch, M.: Periodic solution finder for an impact oscillator with a drift. J. Sound Vib. **267**(4), 893–911 (2003)
10. Chatterjee, S., Mallik, A.K., Ghosh, A.: On impact dampers for non-linear vibrating systems. J. Sound Vib. **187**(3), 403–420 (1995)
11. Barrientos, G., Baeza, L.: Simulation of impact between rigid elements. Int. J. Solids Struct. **40**(19), 4943–4954 (2003)
12. Hinrichs, N., Oestreich, M., Popp, K.: Dynamics of oscillators with impact and friction. Chaos Solitons Fractals **8**(4), 535–558 (1997)
13. Hinrichs, N., Oestreich, M., Popp, K.: On the modeling of friction oscillators. J. Sound Vib. **216**(3), 435–459 (1998)
14. Davis, R.B., Virgin, L.N.: Non-linear behavior in a discretely forced oscillator. Int. J. Non-Linear Mech. **42**(5), 744–753 (2007)
15. Batako, A.D.L., Lalor, M.J., Piiroinen, P.T.: Numerical bifurcation analysis of a friction-driven vibro-impact system. J. Sound Vib. **308**, 392–404 (2007)
16. Piiroinen, P.T., Kuznetsov, Y.A.: An event-driven method to simulate Filippov systems with accurate computing of sliding motions. ACM Trans. Math. Softw. **34**(3), Article 13 (2008)
17. Nguyen, V.-D., Woo, K.-C., Pavlovskaia, E.: Experimental study and mathematical modelling of a new of vibro-impact moling device. Int. J. Non-Linear Mech. **43**(6), 542–550 (2008)
18. Barkan, D.D.: Dynamics of Bases and Foundations. McGraw-Hill, New York (1962)
19. Rodger, A.A., Littlejohn, G.S.: A study of vibratory driving in granular soils. Geotechnique **30**, 269–293 (1980)
20. Nguyen, V.-D., Woo, K.-C.: Nonlinear dynamic responses of new electro-vibroimpact system. J. Sound Vib. **310**, 769–775 (2008)
21. Wiercigroch, M., Wojewoda, J., Krivtsov, A.M.: Dynamics of ultrasonic percussive drilling of hard rocks. J. Sound Vib. **280**(3–5), 739–757 (2005)
22. Wiercigroch, M., Sin, V.W.T., Liew, Z.F.K.: Non-reversible dry friction oscillator, design and measurements. Proc. Inst. Mech. Eng., Part C **213**, 527–534 (1999)
23. Mendrela, E.A., Pudlowski, Z.J.: Transients and dynamics in a linear reluctance self-oscillating motor. IEEE Trans. Energy Convers. **7**(1), 183–191 (1992)
24. Mendrela, E.A.: Comparison of the performance of a linear reluctance oscillating motor operating under ac supply with one under dc supply. IEEE Trans. Energy Convers. **14**(3), 328–332 (1999)
25. Nguyen, V.-D., Woo, K.-C.: Optimisation of a solenoid-actuated vibro-impact mechanism for ground moling machines. In: XXXV Summer School-Conference, Advanced Problems in Mechanics, St. Petersburg, Russia, June 20–28. APM (2007)
26. Woo, K.-C., Rodger, A.A., Neilson, R.D., Wiercigroch, M.: Application of the harmonic balance method to ground moling devices operating in periodic regimes. Chaos Solitons Fractals **11**(15), 2515–2525 (2000)

27. Pavlovskaia, E., Wiercigroch, M., Woo, K.-C., Rodger, A.A.: Modelling of a vibro-impact ground moling system by an impact oscillator with a frictional slider. Meccanica **38**(1), 85–97 (2003)
28. Wiercigroch, M.: A note on the switch function for the stick-slip phenomenon. J. Sound Vib. **175**(5), 700–704 (1994)
29. Pavlovskaia, E., Wiercigroch, M., Grebogi, C.: Two-dimensional map for impact oscillator with drift. Phys. Rev. E **70**, 036201 (2004) (10 pages)
30. Wiercigroch, M., Pavlovskaia, E.: Low-dimensional maps for piecewise smooth oscillators. J. Sound Vib. **305**(4–5), 750–771 (2007)
31. Błażejczyk-Okolewska, B., Czolczynski, K., Kapitaniak, T.: Classification principles of types of mechanical systems with impacts—fundamental assumptions and rules. Eur. J. Mech. A/Solids **23**(3), 517–537 (2004)
32. Czolczynski, K., Kapitaniak, T.: Influence of the mass and stiffness ratio on a periodic motion of two impacting oscillators. Chaos Solitons Fractals **17**, 1–110 (2003)
33. de Souza, S.L.T., Batista, A.M., Caldas, I.L., Viana, R.L., Kapitaniak, T.: Noise-induced basin hopping in a vibro-impact system. Chaos Solitons Fractals **32**, 758–767 (2007)
34. Wiercigroch, M., Sin, V.W.T., Li, K.-Y.: Measurement of chaotic vibration in a symmetrically piecewise linear oscillator. Chaos Solitons Fractals **9**(1–2), 209–220 (1998)
35. Lenci, S., Rega, G.: Regular nonlinear dynamics and bifurcations of an impacting system under general periodic excitation. Nonlinear Dyn. **34**(3–4), 249–268 (2003)
36. Lenci, S., Rega, G.: Numerical control of impact dynamics of inverted pendulum through optimal feedback strategies. J. Sound Vib. **236**(3), 505–527 (2000)
37. Yorke, J.A., Nusse, H.E.: Dynamics: Numerical Explorations. Springer, New York (1998)
38. Crandall, S.H., et al.: In: Crandall, S.H. (ed.) Dynamics of Mechanical and Electromechanical Systems. McGraw-Hill, New York (1968)
39. Bryant, P.H.: LyapOde (Version 4), available online at http://inls.ucsd.edu/~pbryant/ (2009)
40. Eckmann, J.P., Ruelle, D.: Ergodic theory of chaos and strange attractors. Rev. Mod. Phys. **57**(3), 617–656 (1985)
41. Ho, J.-H., Woo, K.-C.: Bifurcations in an electro-vibroimpact system with friction. J. Theor. Appl. Mech. **46**(3), 511–520 (2008)